Two-stage melting of an intercomponent Potts long-range order in two dimensions

Feng-Feng Song [1] and Guang-Ming Zhang [1,2,3,*]

[1] *State Key Laboratory of Low-Dimensional Quantum Physics and Department of Physics, Tsinghua University, Beijing 100084, China*

[2] *Collaborative Innovation Center of Quantum Matter, Beijing 100084, China*

[3] *Frontier Science Center for Quantum Information, Beijing 100084, China*

(Received 26 October 2022; revised 27 March 2023; accepted 3 April 2023; published 14 April 2023)

The interplay of topology and competing interactions can induce enriched phases and phase transitions at finite temperatures. We consider a weakly coupled two-dimensional hexatic-nematic XY model with a relative Z_3 Potts degrees of freedom, and apply the matrix product state method to solve this model rigorously. Since the partition function is expressed as a product of two-legged one-dimensional transfer matrix operator, an entanglement entropy of the eigenstate corresponding to the maximal eigenvalue of this transfer operator can be used as a stringent criterion to determine various phase transitions precisely. At low temperatures, the intercomponent Z_3 Potts long-range order (LRO) exists, indicating that the hexatic and nematic fields are locked together and their respective vortices exhibit quasi-LRO. In the hexatic regime, below the BKT transition of the hexatic vortices, the intercomponent Z_3 Potts LRO appears, accompanying the binding of nematic vortices. In the nematic regime, however, the intercomponent Z_3 Potts LRO undergoes a two-stage melting process. An intermediate Potts liquid phase emerges between the Potts ordered and disordered phases, characterized by an algebraic correlation with formation of charge-neutral pairs of both hexatic and nematic vortices. These two-stage phase transitions are associated with the proliferation of the domain walls and vortices of the relative Z_3 Potts variable, respectively. Our results thus provide a prototype example of two-stage melting of a two-dimensional LRO driven by multiple topological defects.

DOI: 10.1103/PhysRevB.107.165129

I. INTRODUCTION

The concept of topological defects has been one of the cornerstones in the study of phase transitions in two-dimensional (2D) systems. The known example is the Berezinskii-Kosterlitz-Thouless (BKT) phase transition [1–3], where unbinding of integer vortices occurs in the absence of spontaneous breaking of continuous symmetry. The followed renormalization group Kosterlitz-Thouless-Halperin-Nelson-Young theory [4–6] describes a two-stage melting process of 2D crystals: dissociation of dislocation pairs induces a BKT-type transition from a crystal phase to a hexatic phase with a quasi-long-range (quasi-LRO) orientational order and a further transition results from unbinding of disclinations, as a dislocation can be represented as a coupled pair of disclinations. Despite four decades of research, it is still challenging to find a simple microscopic model that exhibits these phenomena theoretically [7,8].

Recently, it became known that the interaction of multiple topological excitations also plays a central role in many physical systems ranging from superfluids/superconductors to condensed atom-molecular mixtures [9–16]. Among these studies, a prototype model is a 2D coupled hexatic-nematic XY spin model proposed for an unusual melting process [17,18] and a hidden-order phase transition of isotropic liquid-crystal thin films [19–21]. As shown in Fig. 1(a), the hexatic degrees of freedom describe a sixfold bond-orientational field represented by $\Theta = |\Theta| \exp(i6\vartheta)$, with ϑ as the bond angle linking the centers of mass of neighboring molecules [4], while the nematic degrees of freedom arising from the herringbone order in the crystalline phase [17] are described by $\Phi = |\Phi| \exp(i2\varphi)$. Three inequivalent herringbone patterns are displayed in Fig. 1(b), from which a different herringbone pattern with the same orientation can be obtained by translating over a lattice vector. The Hamiltonian is described by a coupled bilayer system

$$H = -J_2 \sum_{\langle i,j \rangle} \cos(2\varphi_i - 2\varphi_j) - J_6 \sum_{\langle i,j \rangle} \cos(6\vartheta_i - 6\vartheta_j) - K \sum_i \cos(6\vartheta_i - 6\varphi_i), \quad (1)$$

where φ_i and $\vartheta_i \in [0, 2\pi]$ are two $U(1)$ phase fields, J_2 and J_6 are their respective nearest-neighbor intrafield couplings, and the intercomponent coupling K denotes the minimal hexatic-nematic coupling allowed by the relative symmetry [17].

The study of this 2D coupled XY spin model in the context of nematic/hexatic liquid crystalline systems has a very long history, and is plagued with complexities, confusion, and unexplained puzzling results, which have been reviewed in Ref. [21]. In the *strongly* coupled model, large-scale Monte Carlo simulations had determined the possible Z_3 Potts transition relative to the BKT transition [19,20]. In the hexatic regime, the intercomponent Z_3 Potts LRO is developed below the BKT transition of the hexatic vortices, however, in the

*gmzhang@tsinghua.edu.cn

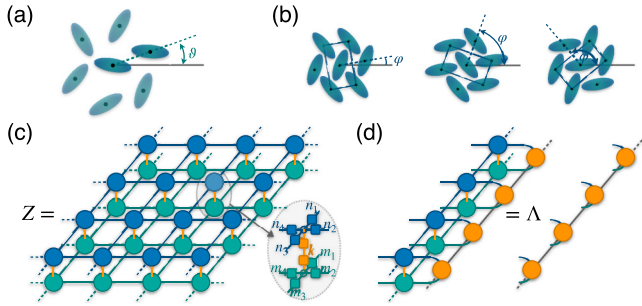

FIG. 1. (a) The bond-orientational angle ϑ joining the centers of neighboring molecules with respect to a laboratory axis. (b) Three possible herringbone patterns. (c) The double-layer tensor network of the partition function and the local tensor. (d) Eigenequation of the 1D transfer operator.

nematic regime the formation of the Z_3 Potts LRO coincides with the BKT vortex binding transition [19,20]. A recent numerical work suggests that the Z_3 Potts LRO in the nematic regime may form above the BKT transition [21]. Due to the lack of sharp thermodynamic signatures associated with the binding of topological defects, the scenario of a single transition cannot be fully excluded. The phase structure in the nematic regime is expected to be revealed only in the *weakly* coupled model, which remains largely unexplored because of the requirements of significantly larger system sizes with enlarged vortex cores.

To resolve this long-standing issue, we apply a state-of-art tensor network method [22–24] to surmount those difficulties. As the partition function of a 2D statistical model can be represented as a product of two-legged 1D transfer operator [Fig. 1(c)], its eigenequation [Fig. 1(d)] can be solved by the algorithm of variational uniform matrix product states (MPS) in the thermodynamic limit [25–28]. According to the singularity displayed by the entanglement entropy for the 1D quantum analog, the various phase transitions in the global phase diagram can be precisely determined [29,30]. In the hexatic regime, we obtain similar results to the previous ones [19–21]. To our surprise, in the nematic regime, we discover that the intercomponent Potts LRO itself undergoes a two-stage melting process. An intermediate Potts liquid phase emerges simultaneously with the formation of charge-neutral pairs of hexatic and nematic vortices. Such two-stage transitions are associated with the separated proliferations of the domain walls and vortices of the Potts variable, respectively. Furthermore, we show that, when increasing the hexatic-nematic coupling strength, the two-stage transitions gradually merge into a single transition, the result for the strongly coupled model [19,20].

II. TENSOR NETWORK METHOD

We first simplify the model Hamiltonian Eq. (1) by introducing new variables $\phi = 2\varphi$ and $\theta = 6\vartheta$,

$$H/J = -\Delta \sum_{\langle i,j\rangle} \cos(\phi_i - \phi_j) - (2-\Delta) \sum_{\langle i,j\rangle} \cos(\theta_i - \theta_j) - \lambda \sum_i \cos(\theta_i - 3\phi_i), \tag{2}$$

where $\lambda = K/J$, $J = (J_2 + J_6)/2$, and $\Delta = J_2/J$ as the relative interacting strength of the hexatic and nematic fields. In the absence of the hexatic-nematic coupling, the model has $U(1) \times U(1)$ symmetry and exhibits two independent BKT phase transitions. For $\lambda \neq 0$, the model is invariant under a $U(1) \times Z_3$ transformation, $\phi_i \to \phi_i + \alpha/3 + 2\pi k_i/3$ and $\theta_i \to \theta_i + \alpha$, where $k_i = 0, 1, 2$ correspond to a Z_3 degrees of freedom. Specially, a sufficiently large λ tends to lock the hexatic and nematic fields, $\theta_i = 3\phi_i$, and the model is reduced to a generalized XY model [31–34].

In the tensor network framework, after a duality transformation, the partition function is expressed as a tensor contraction over all auxiliary links,

$$Z = \mathrm{tTr} \prod_i O^{n_3 m_3, n_4 m_4}_{n_1 m_1, n_2 m_2}(i), \tag{3}$$

where tTr denotes the tensor contraction, which forms a double-layer tensor network shown in Fig. 1(c). Each local tensor O is given by

$$O^{n_3 m_3, n_4 m_4}_{n_1 m_1, n_2 m_2} = \sum_k \left(\prod_{l=1}^{4} I_{n_l}(\beta\Delta) I_{m_l}(\beta(2-\Delta)) \right)^{1/2} \times I_k(\beta\lambda) \delta^{n_3+n_4+3k}_{n_1+n_2} \delta^{m_3+m_4}_{m_1+m_2+k}, \tag{4}$$

where $I_n(x)$ is the modified Bessel function of the first kind, n and m are integers, and $\beta = 1/(k_B T)$. The global $U(1) \times Z_3$ invariance is encoded in the local tensor. In the thermodynamic limit, the partition function is determined by the dominant eigenvalues of the 1D quantum transfer operator $\hat{T}$, whose eigenequation [Fig. 1(d)] $\hat{T}|\Psi(A)\rangle = \Lambda_{\max}|\Psi(A)\rangle$ can be accurately solved by the algorithm of variational uniform MPS [25–28]. The corresponding 1D quantum Hamiltonian is $\hat{H}_{1D} = -(1/\beta)\ln\hat{T}$, and the leading eigenvector $|\Psi(A)\rangle$ is represented by an MPS whose precision is controlled by the auxiliary bond dimension D of the local tensors.

From the maximal eigenvalue and its eigenvector of the 1D quantum transfer operator, various physical quantities can be estimated accurately [29,30,35,36]. As the phase transitions are concerned, the quantum entanglement entropy is the most efficient measure [37,38], which can be directly determined via the Schmidt decomposition: $S_E = -\sum_{\alpha=1}^{D} s_\alpha^2 \ln s_\alpha^2$ with s_α as the singular values from the bipartition of the state $|\Psi(A)\rangle$. Various two-point correlation functions can be evaluated by the trace of an infinite sequence of channel operators containing two local impurity tensors, and the detailed formulation can be found in Appendices A–C.

The superfluid response is described by the spin stiffness as the second derivative of the free energy density $f = -(1/N\beta)\ln Z$ with respect to a twist v along a reference direction: $\rho_s = \frac{\partial^2 f}{\partial^2 v}|_{v=0}$. The twist needs to be imposed in a way that respects the joint $U(1)$ invariance of the hexatic and nematic fields as

$$(\phi_i, \theta_i) \to (\phi_i + \vec{v}\cdot\vec{r}_i, \theta_i + 3\vec{v}\cdot\vec{r}_i), \tag{5}$$

where $\vec{r}_i$ is the position vector for the lattice site i and $\vec{v}$ is a constant vector to increase the phase difference across each neighboring hexatic spins three times larger than nematic spins. So, the jump of spin stiffness is altered from the BKT predictions when the unbinding of the θ and ϕ vortices

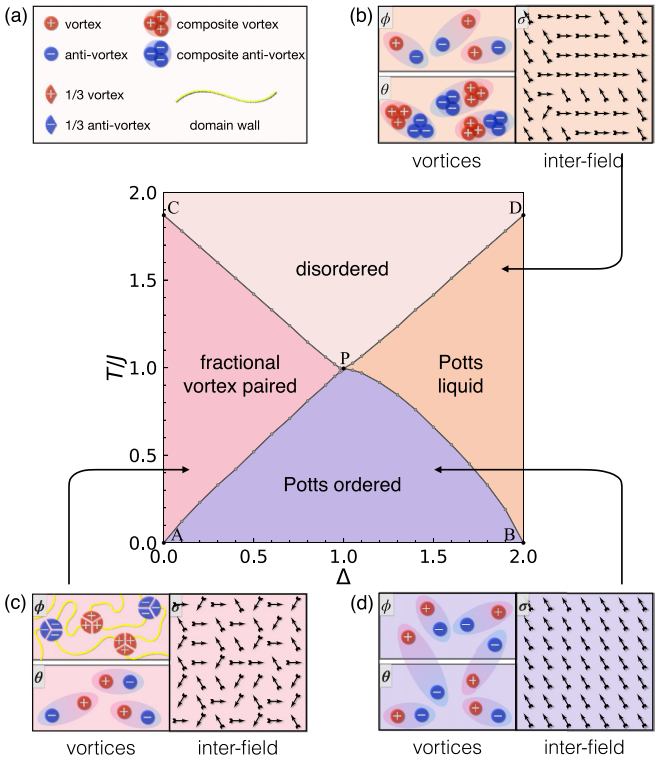

FIG. 2. The global phase diagram of the weakly coupled hexatic-nematic XY model with a typical coupling $\lambda = 0.1$. (a) Schematic pictures of different topological excitations. (b) In the Potts liquid phase, the intercomponent Potts variable has quasi-LRO, the vortex-antivortex pairs in ϕ fields are formed, and the dominant topological defects of the θ fields are composite vortex pairs with charge $q_\theta = \pm 3$. (c) In the fractional vortex paired phase, the θ vortices have quasi-LRO and the ϕ vortices are fractionalized as paired vortices with charge $q_\phi = 1/3$. (d) In the Potts ordered phase, vortices in both types are bound in pairs, accompanying the intercomponent Potts LRO.

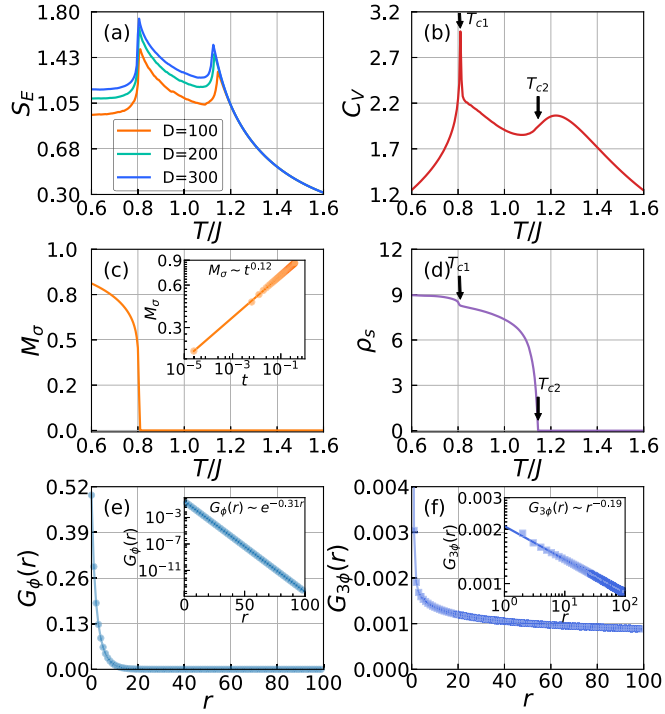

FIG. 3. The numerical results for $\Delta = 0.8$ and $\lambda = 0.1$. (a) The entanglement entropy. (b) The specific heat. (c) The magnetization of the Potts variable. In the inset t is the reduced temperature $t = |T_{c1} - T|/T_{c1}$. (d) The superfluid stiffness. (e), (f) At $T = 1.0J$, the correlation function $G_\phi(r)$ for $q_\phi = 1$ vortices decays exponentially, but the correlation function $G_{3\phi}(r)$ for $q_\phi = 1/3$ vortices decays in power law.

happens separately [39]. The detailed calculations are given in Appendix D.

The hexatic-nematic XY model has a rich physics, and the most intriguing results are expected in the weakly coupled case. For a typical value of $\lambda = 0.1$, a global phase diagram is derived in Fig. 2. All phase boundaries are determined by the singularity displayed in the entanglement entropy S_E for the 1D quantum transfer operator. Since the succession of phases crucially depends on the intracomponent coupling ratio, our results are discussed in hexatic $\Delta < 1$ and nematic $\Delta > 1$ regimes, separately.

III. PHASE TRANSITIONS IN THE HEXATIC REGIME

For a typical value $\Delta = 0.8$, our numerical results show two singular peaks in the entanglement entropy at $T_{c1} \simeq 0.805J$ and $T_{c2} \simeq 1.145J$, respectively, as shown in Fig. 3(a). The peak positions are nearly unchanged with increasing bond dimensions $D = 100, 200, 300$, so the transition points are determined with high accuracy. The corresponding specific heat is shown in Fig. 3(b), exhibiting a sharp divergence at T_{c1} and a small rounded bump around T_{c2}. The maximum of the hump is above T_{c2}, a typical feature of the BKT transition [2,3], while the low-T singular behavior is fitted by $C_V \propto |T - T_{c1}|^\alpha$ with $\alpha \simeq 1/3$. Further evidence is provided by a Z_3 order parameter $M_\sigma = \langle \cos(\sigma_i) \rangle$ with $\sigma_i = \theta_i/3 - \phi_i$. As shown in Fig. 3(c), M_σ becomes finite at T_{c1}, suggesting that a true LRO is established and the relative phase between the ϕ and θ fields is fully locked. The magnetization satisfies the scaling form $M_\sigma \propto (T_{c1} - T)^\beta$ with the critical exponent $\beta \simeq 1/9$. These critical exponents are perfectly in agreement with the Z_3 Potts transition [40].

As shown in Fig. 3(d), the spin stiffness starts to dramatically increase from zero at the BKT transition T_{c2}. When the temperature further decreases, a small jump appears to enhance the spin stiffness at the Potts transition T_{c1} precisely. Such a small increase of spin stiffness results from bindings of integer ϕ vortices [21,33]. When cooling the system from the disordered phase, the correlation function $G_\theta(r) = \langle \cos(\theta_i - \theta_{i+r}) \rangle$ exhibits a power-law decay at T_{c2}, indicating the binding of hexatic vortices. In the intermediate temperature regime ($T_{c1} < T < T_{c2}$), we found that $G_\phi(r) = \langle \cos(\phi_i - \phi_{i+r}) \rangle$ decays exponentially, but $G_{3\phi}(r)$ exhibits an algebraic correlation. In Figs. 3(e) and 3(f), a direct comparison at $T = 1.0J$ suggests that the vortices are fractionalized into the $q_\phi = 1/3$ vortices. As the correlation length ξ_ϕ extracted from $G_\phi(r)$ follows an exponentially divergence above T_{c1}, we thus conclude that the low-temperature transition is

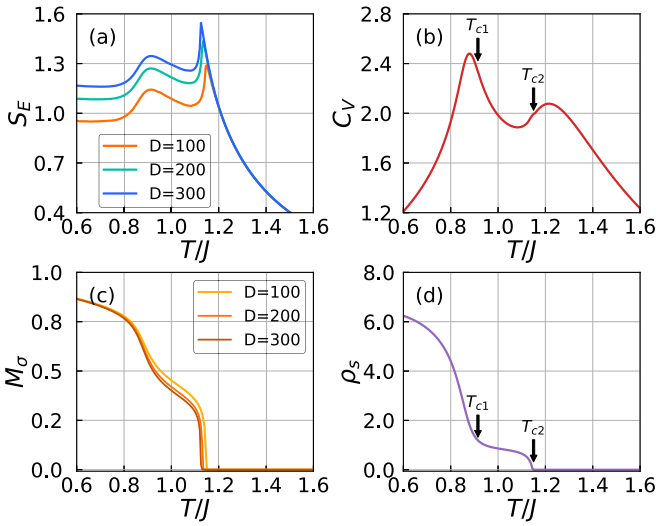

FIG. 4. The numerical results for $\Delta = 1.2$ with $\lambda = 0.1$. (a) The entanglement entropy. (b) The specific heat. (c) The Potts magnetization. (d) The superfluid stiffness.

a hybrid BKT and Potts transition. The detailed numerical results are included in Appendix E.

IV. PHASE TRANSITIONS IN THE NEMATIC REGIME

For a typical value $\Delta = 1.2$, our numerical calculations show two peaks in the entanglement entropy at $T_{c1} \simeq 0.915J$ and $T_{c2} \simeq 1.15J$, respectively, as seen in Fig. 4(a). Unlike the strongly coupled model [21], the specific heat C_V exhibits a pronounced peak at T_{c1} and a bump at T_{c2}, as displayed in Fig. 4(b). The bump appears slightly above T_{c2} as the usual BKT transition, but the peak locates below T_{c1}. Surprisingly, the magnetization of the relative Potts variable displays a two-step feature below T_{c2}, as shown in Fig. 4(c). The artificial finite Potts magnetization in the intermediate phase is due to the finite-bond dimension effect, which should decrease slowly to zero with increasing bond dimensions in MPS approximations for $U(1)$ phases [28,29]. To figure out the transition at T_{c1}, we calculate the superfluid stiffness, which also has a two-step jump, as displayed in Fig. 4(d). In contrast to the hexatic regime, the stiffness drops more dramatically at T_{c1} than at T_{c2}. Since the phase twist $\vec{v}$ applied to the hexatic θ field is three times larger than that of the nematic ϕ field, the first drop of the stiffness is nearly six times larger than the second drop.

The abrupt drop of spin stiffness at T_{c1} is rather rare, and the binding of charge-neutral vortex pairs of θ field can be ruled out from the correlation function $G_\theta(r) = \langle \cos(\theta_i - \theta_{i+r}) \rangle$. On two sides of T_{c1}, the $G_\theta(r)$ correlations have the power-law behavior as shown in Figs. 5(a) and 5(c), indicating that the quasi-LRO persists through the transition. As displayed in Fig. 5(e), a direct comparison between the amplitudes of $G_\theta(r) \sim r^{-\eta_\theta}$ at $r = 100$ indicates that the correlation above T_{c1} is greatly suppressed by three orders of magnitude, and the exponent η_θ varies with temperature depicted in the inset. The extremely weak correlation above T_{c1} may account for the dramatic jump in total stiffness at T_{c1}. Below T_{c2}, the onset of algebraic correlations of the ϕ vortices also

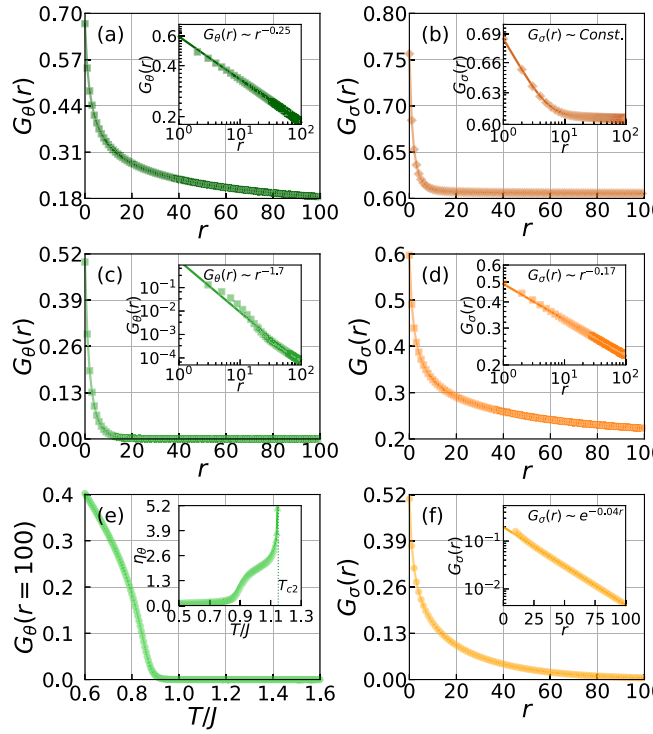

FIG. 5. (a), (c) The correlation functions $G_\theta(r)$ in both the Potts ordered phase ($T = 0.8J$) and the Potts liquid phase ($T = 1.0J$). (e) The correlation $G_\theta(r)$ at $r = 100$ and the exponents in the inset. (b), (d), (f) The correlation functions $G_\sigma(r)$ in the Potts ordered, Potts liquid, and disordered phases.

induces the quasi-LRO of the θ vortices. So, the dominant topological excitations between T_{c1} and T_{c2} are composite vortex pairs of $q_\theta = 3$ with an internal structure of three bound vortices.

By calculating the correlations of the relative Z_3 Potts variable, we find that the inter-component Potts order-disorder phase transition splits into two different transitions separated by an intermediate liquid phase with quasi-LRO correlation. As shown in Figs. 5(b), 5(d), and 5(f), the correlation function $G_\sigma(r)$ exhibits a LRO in the Potts ordered phase, an algebraic decay in the intermediate phase, and an exponential decay in the Potts disordered phase, respectively. Actually the Potts quasi-LRO occurs simultaneously with the formation of charge-neutral pairs of hexatic and nematic vortices. Moreover, the correlation length for Potts variables displays a similar structure as the p-state clock model with $p > 4$, and the detailed discussions are given in Appendix F.

Unlike the 2D Ising model, the excitations in the Z_3 Potts model include both the looplike domain walls and vortices, and the usual Potts transition results from a coupled proliferation of two topological defects [41]. However, a quasi-LRO phase appears in a generalized Z_3 Potts model by artificially raising the vortex core energy [42]. We notice that the effective core energy of Z_3 vortices in the coupled hexatic-nematic model is related to the hexatic-nematic coupling. A larger λ makes the excitations of free vortices in the θ field more costly, and the domain-wall energy increases dramatically to forbid the pre-excitations of domain walls. However, a small λ is required to achieve a relatively high ratio of the core energy

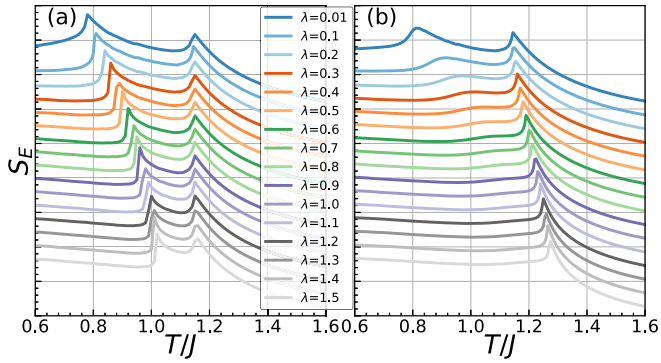

FIG. 6. The entanglement entropy for different λ in the hexatic regime (a) $\Delta = 0.8$ and the nematic regime (b) $\Delta = 1.2$. For a good comparison, each curve is relatively shifted by $\Delta S_E = 0.2$. The displayed results are obtained under MPS bond dimension $D = 100$.

of the Z_3 vortices. To illustrate this physics, we calculated the entanglement entropy as a function of temperature for different values of λ. As shown in Fig. 6, in the hexatic regime ($\Delta = 0.8$), the entanglement entropy results indicate that the model always has two phase transitions similar to those of the strongly coupled model, while in the nematic regime ($\Delta = 1.2$), two-stage phase transitions are allowed only for a small λ value. As λ increases, the intermediate Potts liquid phase obscures because the lower transition gets vague and two transitions are merged together.

V. CONCLUSION AND OUTLOOK

We have studied a weakly coupled hexatic-nematic XY model by using the tensor-network method. It is found that the hexatic regime shares a similar phase structure to that of the strongly coupled model [19–21]. In the nematic regime, however, an intercomponent Z_3 Potts liquid phase emerges as the intermediate phase of the two-stage melting of the Potts LRO. Actually, this emergent Potts liquid phase opens up a promising route towards better understanding the hidden structure of the phase transitions driven by different topological defects. Such an intriguing splitting of phase transitions should exist in other systems with multiple topological excitations, such as multistage melting process of 2D liquid crystal films [43–45]. Above the melting of positional order, the orientational order itself possesses a further structure. Future study can be extended to the coupled $U(1) \times Z_n$ systems with larger n where a richer phase diagram is expected [46]. Moreover, in various XY systems like condensed atom-molecular mixtures and multicomponent superfluids/superconductors [47–50], such unconventional phenomena should also be realizable.

ACKNOWLEDGMENT

The research is supported by the National Key Research and Development Program of MOST of China (2017YFA0302902).

APPENDIX A: TENSOR NETWORK REPRESENTATION OF OUR MODEL

A good wealth of fascinating physics have been found in many-body systems but the numerical treatment still remains challenging due to the nature of strong correlations. Tensor networks (TNs) have proven to be a very efficient tool to overcome these challenges based on the variational ansatz wave functions. Due to the unique advantages of faithfully capturing the entanglement structure of many-body states, they are increasingly becoming a standard tool for not only strongly correlated quantum systems but also many-body classical problems.

The central but often nontrivial task in condensed matter physics is to evaluate the partition function of a system. To implement the TN method in the coupled hexatic-nematic XY model, the first step is to convert the classical lattice model with nearest-neighbor local interactions into a TN representation. The coupled hexatic-nematic XY model on a 2D square lattice is defined by the Hamiltonian

$$H = -J_2 \sum_{\langle i,j \rangle} \cos(2\varphi_i - 2\varphi_j) - J_6 \sum_{\langle i,j \rangle} \cos(6\vartheta_i - 6\vartheta_j) - K \sum_i \cos(6\vartheta_i - 6\varphi_i), \tag{A1}$$

where $\langle i, j \rangle$ refers to nearest neighbors, φ_i and $\vartheta_i \in [0, 2\pi]$ are phase angles associated to the lattice site i, J_2 and J_6 are their respective intracomponent coupling strengths, and K denotes the intercomponent coupling. To lowest order in φ and ϑ by introducing $\phi = 2\varphi$ and $\theta = 6\vartheta$, the simplified Hamiltonian in the same universality class can be written as

$$H/J = -\sum_{\langle i,j \rangle} \Delta \cos(\phi_i - \phi_j) - (2 - \Delta) \sum_{\langle i,j \rangle} \cos(\theta_i - \theta_j) - \lambda \sum_i \cos(\theta_i - 3\phi_i), \tag{A2}$$

where $J = \frac{1}{2}(J_2 + J_6)$, $\lambda = K/J$ and $\Delta = J_2/J \in [0, 2]$ tuning the relative strength of hexatic and nematic interactions.

To derive the TN representation, we express the partition function on its original lattice and the Boltzmann weights are represented as a tensor product of local bonds as shown in Fig. 7(a),

$$Z = \iint \frac{d\phi_i d\theta_i}{(2\pi)^2} \prod_{\langle i,j \rangle} W_U(\phi_i, \phi_j) W_I(\phi_i, \theta_i) W_L(\theta_i, \theta_j), \tag{A3}$$

where

$$W_U(\phi_i, \phi_j) = e^{\beta \Delta \cos(\phi_i - \phi_j)}, \tag{A4}$$

$$W_I(\phi_i, \theta_i) = e^{\beta \lambda \cos(\theta_i - 3\phi_i)}, \tag{A5}$$

$$W_L(\theta_i, \theta_j) = e^{\beta (2-\Delta) \cos(\theta_i - \theta_j)} \tag{A6}$$

can be viewed as infinite matrices whose indices are the continuous ϕ and θ variables. The partition function is now cast into a double-layer TN representation, where the integrations of $\int d\phi/2\pi$ and $\int d\theta_i/2\pi$ are denoted as blue and green dots and the matrix indices take the same values at the joint points.

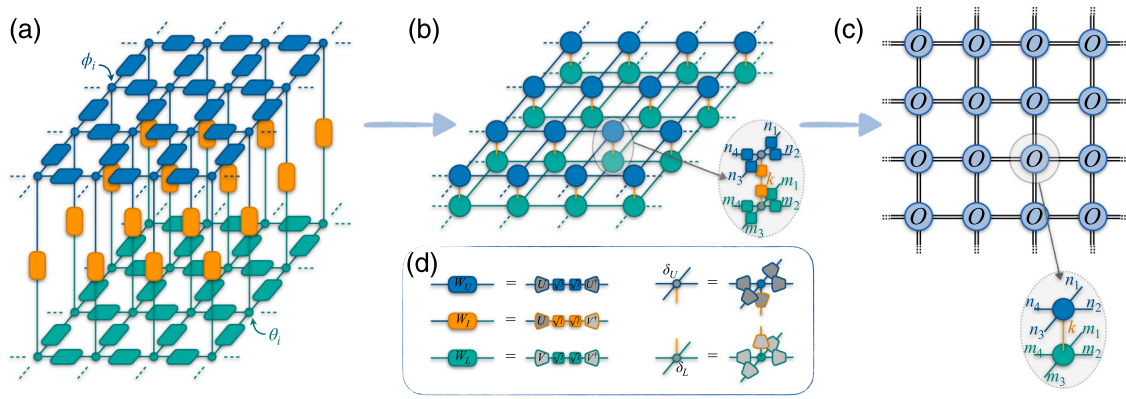

FIG. 7. (a) Tensor network representation of the partition function with Boltzmann weights represented as a tensor product of local bonds. (b) The double-layer TN derived in the main text. (c) The 2D uniform tensor network representation of the partition function. (d) The eigenvalue decompositions of the symmetric matrix W and the transformation to discrete degrees of freedom.

The duality transformation changes the local tensors from continuous $U(1)$ variables onto a discrete basis for further numerical analysis. As shown in Fig. 7(d), we perform the character expansion for the symmetric matrix W,

$$W_U(\phi_i,\phi_j)=\sum_n U_{\phi_i,n}\, I_n(\beta\Delta)\, U^*_{\phi_j,n}, \tag{A7}$$

$$W_I(\phi_i,\theta_i)=\sum_k U_{\phi_i,-3k}\, I_k(\beta\lambda)\, V^*_{\theta_i,k}, \tag{A8}$$

$$W_L(\theta_i,\theta_j)=\sum_m V_{\theta_i,m}\, I_m(\beta(2-\Delta))\, V^*_{\theta_j,m}, \tag{A9}$$

where $U_{\phi_i,n}=e^{in\phi_i}$, $V_{\theta_i,m}=e^{im\theta_i}$, and the diagonal $I_n(x), I_m(x), I_k(x)$ are the modified Bessel functions of the first kind.

Then, as displayed in Fig. 7(d), we can simply integrate out the $U(1)$ phase variables at each site by a Fourier transformation

$$\int\frac{d\phi_i}{2\pi}U_{\phi_i,n_1}U_{\phi_i,n_2}U^*_{\phi_i,n_3}U^*_{\phi_i,n_4}U_{\phi_i,-3k}=\delta^{n_3+n_4+3k}_{n_1+n_2}\equiv\delta_U, \tag{A10}$$

$$\int\frac{d\theta_i}{2\pi}V_{\theta_i,m_1}V_{\theta_i,m_2}V^*_{\theta_i,m_3}V^*_{\theta_i,m_4}V_{\theta_i,k}=\delta^{m_3+m_4}_{m_1+m_2+k}\equiv\delta_L. \tag{A11}$$

In this way, the continuous variables ϕ and θ are now transformed into the discrete bond indices n, m, and k. Moreover, we evenly divide the diagonal I tensors and take a contraction of the $\sqrt{I}$ tensors connecting to the respective δ tensors. As a result, the double-layer TN representation of the partition function in the main text is obtained as shown in Fig. 7(b). The local tensor O can then be obtained by grouping the corresponding tensor indices in the upper and lower layers and summing out the interlayer k indices:

$$O^{n_3m_3,n_4m_4}_{n_1m_1,n_2m_2}=\sum_k\left(\prod_{l=1}^4 I_{n_l}(\beta\Delta)I_{m_l}(\beta(2-\Delta))\right)^{1/2}\times I_k(\beta\lambda)\,\delta^{n_3+n_4+3k}_{n_1+n_2}\delta^{m_3+m_4}_{m_1+m_2+k}. \tag{A12}$$

And, finally, the partition function is now successfully converted into a uniform TN on the 2D square lattice as displayed in Fig. 7(c),

$$Z=\mathrm{tTr}\prod_i O^{n_3m_3,n_4m_4}_{n_1m_1,n_2m_2}(i), \tag{A13}$$

where tTr denotes the sum over all auxiliary bond indices. The symmetries of the original model are well preserved in the TN representation. It is evident that the global $U(1)\times Z_3$ invariance of the bilayer model is encoded in each local tensor since $O^{n_3m_3,n_4m_4}_{n_1m_1,n_2m_2}\neq 0$ only if $n_1+3m_1+n_2+3m_2=n_3+3m_3+n_4+3m_4$.

As a matter of fact, the equivalence of the Hamiltonian Eqs. (A1) and (A2) can be easily verified from the perspective of local tensors. The duality transformation can be performed on φ and ϑ in the same way for Hamiltonian Eq. (A1), and the integration will generate the same local tensor as

$$\int\frac{d\varphi_i}{2\pi}e^{i2n_1\varphi_i}e^{i2n_2\varphi_i}e^{-i2n_3\varphi_i}e^{-i2n_4\varphi_i}e^{-i6k\varphi_i}=\delta^{2n_3+2n_4+6k}_{2n_1+2n_2}=\delta^{n_3+n_4+3k}_{n_1+n_2}\equiv\delta_U, \tag{A14}$$

$$\int\frac{d\vartheta_i}{2\pi}e^{i6m_1\vartheta_i}e^{i6m_2\vartheta_i}e^{-i6m_3\vartheta_i}e^{-i6m_4\vartheta_i}e^{-i6k\vartheta_i}=\delta^{6m_3+6m_4}_{6m_1+6m_2+6k}=\delta^{m_3+m_4}_{m_1+m_2+k}\equiv\delta_L. \tag{A15}$$

Therefore, all the physical quantities deducted from the partition function should be the same for both Eqs. (A1) and (A2).

APPENDIX B: ALGORITHM OF UNIFORM MATRIX PRODUCT STATES

Although it is often straightforward to write the TN representation for the many-body problem, the real challenge for numerical simulations comes from the contraction of the whole tensor network which is proved to be NP hard when the network is complicated. Fortunately, a lot of algorithms have been proposed to contract an infinite translation-invariant TN. One of the best practices to address the challenge is the algorithm of uniform matrix product states [25–27], which greatly speeds up the process of finding the leading eigenvector of the transfer matrix based on a variational ansatz.

Here we provide a brief review of this efficient algorithm based on a set of optimized eigensolvers. In the

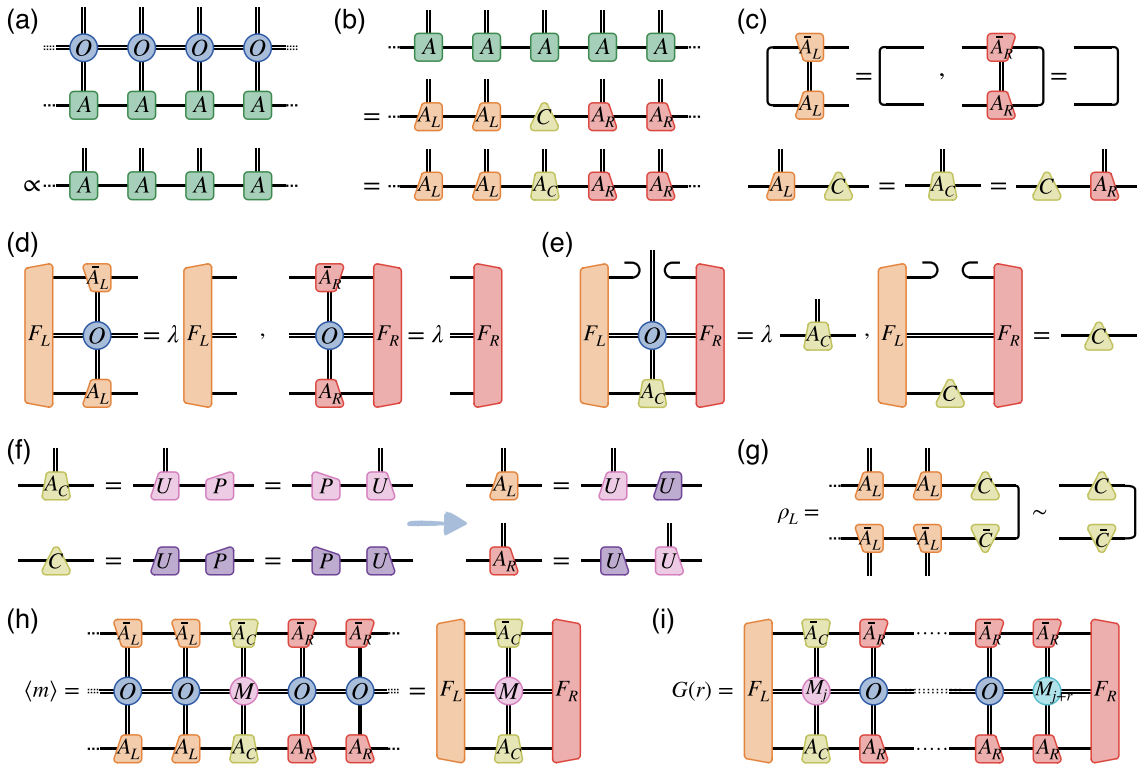

FIG. 8. (a) Eigenequation for the fixed-point uMPS of the transfer operator T. (b) The uniform representation and two equivalent mixed canonical forms of the fixed-point uMPS. (c) The canonical conditions of the fixed-point local tensors and the isometric gauge transformation between them. (d) Eigenequations to update the left and right environmental eigenvectors of the channel operators. (e) Eigenequations to obtain the central tensors based on the new environment. (f) Polar decompositions to get the left and right canonical local tensors from the central tensors. (g) The reduced density matrix obtained by tracing out the right part of the uMPS. (h) Expectation value of a local observable by contracting the leading eigenvectors of the channel operators. (i) Two-point correlation function expressed by contracting a sequence of channel operators.

thermodynamic limit, the partition function is determined by the dominant eigenvalues of the 1D quantum transfer operator $\hat{T}$, whose eigenequation is shown in Fig. 8(a):

$$\hat{T}|\Psi(A)\rangle = \Lambda_{\max}|\Psi(A)\rangle. \tag{B1}$$

For a translation-invariant system, the leading eigenvector of the transfer matrix can be expressed as the uniform matrix product states (uMPS),

$$|\Psi(A)\rangle = \sum_{\{(n_i m_i)\}} \mathrm{Tr}(\cdots A^{(n_1 m_1)} A^{(n_2 m_2)} A^{(n_3 m_3)} \cdots), \tag{B2}$$

which is constructed by infinitely many repetitions of rank-3 $A^{(n_i m_i)}_{\alpha\beta}$ with auxiliary bond dimension $\alpha, \beta = 1, 2, \ldots, D$. Here, D is the upper bond dimension which controls the accuracy of the approximations. As shown in Fig. 8(b), to fix the gauge of the uMPS, we should bring the uMPS into the equivalent mixed canonical forms as

$$|\Psi\rangle = \sum_{\alpha,\beta=1}^{D} C_{\alpha,\beta} \left|\Psi_\alpha^{[-\infty,(n_j m_j)]}\right\rangle \otimes \left|\Psi_\beta^{[(n_{j+1} m_{j+1}),+\infty]}\right\rangle \tag{B3}$$

and

$$|\Psi\rangle = \sum_{\alpha,\beta=1}^{D} \left(A_C^{(n_j m_j)}\right)_{\alpha,\beta} \left|\Psi_\alpha^{[-\infty,(n_{j-1} m_{j-1})]}\right\rangle \otimes \left|\Psi_\beta^{[(n_{j+1} m_{j+1}),+\infty]}\right\rangle, \tag{B4}$$

where $|\Psi_\alpha^{[-\infty,(n_j m_j)]}\rangle$ and $|\Psi_\beta^{[(n_{j+1} m_{j+1}),+\infty]}\rangle$ are the left and right orthonormal bases comprised of the left and right canonical local tensors

$$\left|\Psi_\alpha^{[-\infty,(n_j m_j)]}\right\rangle = \sum_{\{(n_i m_i)\}} \mathrm{Tr}\left(\cdots A_L^{(n_{j-1} m_{j-1})} A_L^{(n_j m_j)}\right), \tag{B5}$$

$$\left|\Psi_\beta^{[(n_{j+1} m_{j+1}),+\infty]}\right\rangle = \sum_{\{(n_i m_i)\}} \mathrm{Tr}\left(A_R^{(n_{j+1} m_{j+1})} A_R^{(n_{j+2} m_{j+2})} \cdots\right). \tag{B6}$$

The left and right orthonormal tensors A_L and A_R satisfy the isometric constraints as displayed in Fig. 8(c):

$$\sum_{(nm)} \left(A_L^{(nm)}\right)^\dagger A_L^{(nm)} = \mathcal{I}, \tag{B7}$$

$$\sum_{(nm)} A_R^{(nm)} \left(A_R^{(nm)}\right)^\dagger = \mathcal{I}. \tag{B8}$$

Another fixed point equation is obtained by pulling the central tensor from right to left:

$$A_C^{(nm)} = A_L^{(nm)} C = C A_R^{(nm)}. \tag{B9}$$

The VUMPS algorithm contains three key steps summarized in Figs. 8(d)–8(f) to find the fixed-point tensors A_L, A_R, and C of the transfer operator $\hat{T}$. These three steps Figs. 8(d)–8(f) are repeated sequentially until the error is less than a given convergence threshold.

(1) As shown in Fig. 8(d), we calculate the left and right environments F_L and F_R by solving the eigenvalue equation with the Arnoldi method,

$$\mathbb{T}_L F_L = \lambda F_L, \tag{B10}$$

$$\mathbb{T}_R F_R = \lambda F_R, \tag{B11}$$

where $\mathbb{T}_L$ and $\mathbb{T}_R$ are the channel operators of A_L and A_R.

(2) As shown in Fig. 8(e), we calculate the central tensors A_C and C based on the new environment by the Arnoldi method,

$$H_{A_C} A_C = \lambda A_C, \tag{B12}$$

$$H_C C = C, \tag{B13}$$

where H_{A_C} and H_C are the effective environment comprised of the updated F_L and F_R.

(3) As shown in Fig. 8(f), we use the left and right polar decompositions of new A_C and C to update A_L and A_R satisfying the isometric conditions

$$A_C = U_{A_C}^{[l]} P_{A_C}^{[l]} = P_{A_C}^{[r]} U_{A_C}^{[r]}, \tag{B14}$$

$$C = U_C^{[l]} P_C^{[l]} = P_C^{[r]} U_C^{[r]}, \tag{B15}$$

where $U_{A_C}^{[l]}$, $U_{A_C}^{[r]}$, $U_C^{[l]}$, and $U_C^{[r]}$ are unitary matrices, and the matrices $P_{A_C}^{[l]}$, $P_{A_C}^{[r]}$, $P_C^{[l]}$ and $P_C^{[r]}$ are Hermitian and positive. Finally, we obtain

$$A_L = U_{A_C}^{[l]} U_C^{[l]\dagger}, \tag{B16}$$

$$A_R = U_C^{[r]\dagger} U_{A_C}^{[r]}. \tag{B17}$$

Actually, the row-to-row transfer matrix should play the same role as the matrix product operator for the 1D quantum spin chains whose logarithmic form can be mapped to a 1D quantum system with complicated interactions. With such a correspondence, the finite-temperature properties of the 2D statistical problem are related to a 1D quantum model at zero temperature and all the low-temperature physics can be achieved from the fixed-point uMPS.

APPENDIX C: CALCULATIONS OF PHYSICAL QUANTITIES

Once the fixed-point uMPS is achieved, various physical quantities can be precisely calculated because the 2D network can be easily squeezed into a 1D chain of channel operators based on the fixed uMPS.

By mapping the transfer matrix to a 1D quantum transfer operator, we bring to it modern concepts of quantum entanglement, while also taking advantage of the sharp criterion for detecting various phase transitions. As shown in Fig. 8(g), we perform a bipartition on the MPS and trace out the right part using the right canonical condition. Since the $|\Psi^{[-\infty,(n_j m_j)]}\rangle$ also forms a unitary basis, the reduced density matrix ρ_L of the left part is expressed as

$$\rho_L = \mathrm{Tr}_R |\Psi\rangle\langle\Psi| = |\Psi^{[-\infty,(n_j m_j)]}\rangle C C^\dagger \langle\Psi^{[-\infty,(n_j m_j)]}| \sim C C^\dagger. \tag{C1}$$

And the entanglement entropy [37] is readily obtained by

$$S_E = -\mathrm{Tr}\,(\rho_L \ln \rho_L) = -\sum_{\alpha=1}^{D} s_\alpha^2 \ln s_\alpha^2, \tag{C2}$$

where s_α are the singular values of the C matrix.

With the fixed-point uMPS, the contraction of an infinite 2D tensor network can be reduced to the trace of an infinite 1D chain of channel operators. The expectation value of of a single-site observable $m(\phi_j, \theta_j)$,

$$\langle m(\phi_j,\theta_j)\rangle = \frac{1}{Z}\prod_i \iint \frac{d\phi_i d\theta_i}{(2\pi)^2} \prod_{\langle i,j\rangle} e^{\beta\Delta\cos(\phi_i-\phi_j)} \times e^{\beta(2-\Delta)\cos(\theta_i-\theta_j)} e^{\beta\lambda\cos(\theta_i-3\phi_i)} m(\phi_j,\theta_j), \tag{C3}$$

can be obtained by the contraction of a reduced network containing an impurity tensor thanks to the fixed-point environment tensors F_L and F_R as displayed in Fig. 8(h),

$$\langle m\rangle = \mathrm{Tr}(\cdots \mathbb{T}_L \mathbb{T}_L \mathbb{T}_M \mathbb{T}_R \mathbb{T}_R \cdots) = \langle F_L|\mathbb{T}_M|F_R\rangle, \tag{C4}$$

where $\mathbb{T}_M = \mathrm{tTr}(A_C \otimes M \otimes \bar{A}_C)$. And the corresponding impurity tensor M can be achieved by

$$M_{n_1 m_1, n_2 m_2}^{n_3 m_3, n_4 m_4} = \sum_k \left(\prod_{l=1}^4 I_{n_l}(\beta\Delta) I_{m_l}(\beta(2-\Delta))\right)^{1/2} I_k(\beta\lambda) \times \iint \frac{d\phi d\theta}{(2\pi)^2} e^{i\phi(n_1+n_2-n_3-n_4-3k)} \times e^{i\theta(m_1+m_2+k-m_3-m_4)} m(\phi,\theta). \tag{C5}$$

For instance, the corresponding impurity tensors for $m_\phi = e^{i\phi}$, $m_\theta = e^{i\theta}$, and $m_\sigma = e^{i(\theta/3-\phi)}$ are

$$(M_\phi)_{n_1 m_1, n_2 m_2}^{n_3 m_3, n_4 m_4} = \sum_k \left(\prod_{l=1}^4 I_{n_l}(\beta\Delta) I_{m_l}(\beta(2-\Delta))\right)^{1/2} \times I_k(\beta\lambda)\, \delta_{n_1+n_2+1}^{n_3+n_4+3k} \delta_{m_1+m_2+k}^{m_3+m_4}, \tag{C6}$$

$$(M_\theta)_{n_1 m_1, n_2 m_2}^{n_3 m_3, n_4 m_4} = \sum_k \left(\prod_{l=1}^4 I_{n_l}(\beta\Delta) I_{m_l}(\beta(2-\Delta))\right)^{1/2} \times I_k(\beta\lambda)\, \delta_{n_1+n_2}^{n_3+n_4+3k} \delta_{m_1+m_2+k+1}^{m_3+m_4}, \tag{C7}$$

$$(M_\sigma)_{n_1 m_1, n_2 m_2}^{n_3 m_3, n_4 m_4} = \sum_k \left(\prod_{l=1}^4 I_{n_l}(\beta\Delta) I_{m_l}(\beta(2-\Delta))\right)^{1/2} \times I_k(\beta\lambda)\, \delta_{n_1+n_2}^{n_3+n_4+3k+1} \frac{\sqrt{3}}{2\pi} \frac{(-1)^l}{l+1/3}, \tag{C8}$$

where $l = m_1 + m_2 + k - m_3 - m_4$.

Moreover, the two-point correlation function $G(r) = \langle m_j m_{j+r}\rangle$ between local observables $m_j(\phi_j, \theta_j)$ and $m_{j+r}(\phi_{j+r}, \theta_{j+r})$,

$$G(r) = \frac{1}{Z}\prod_i \iint \frac{d\phi_i d\theta_i}{(2\pi)^2} \prod_{\langle i,j\rangle} e^{\beta\Delta\cos(\phi_i-\phi_j)} e^{\beta(2-\Delta)\cos(\theta_i-\theta_j)} \times e^{\beta\lambda\cos(\theta_i-3\phi_i)} m_j(\phi_j,\theta_j) m_{j+r}(\phi_{j+r},\theta_{j+r}), \quad \text{(C9)}$$

can be calculated in the same way as a contraction of a 1D chain with two local impurity tensors M_j and M_{j+r} as shown in Fig. 8(i),

$$G(r) = \langle F_L|\mathbb{T}_{M_j}\underbrace{\mathbb{T}_R\cdots\mathbb{T}_R}_{r-1}\mathbb{T}_{M_{j+r}}|F_R\rangle, \quad \text{(C10)}$$

where $\mathbb{T}_{M_j} = \mathrm{tTr}(A_C \otimes M_j \otimes \bar{A}_C)$ and $\mathbb{T}_{M_{j+r}} = \mathrm{tTr}(A_R \otimes M_{j+r} \otimes \bar{A}_R)$.

APPENDIX D: PARTICULAR CALCULATION OF SPIN STIFFNESS

Although there is no local order parameter due to the absence of the $U(1)$ symmetry breaking, the onset of the superfluidity of the hexatic-nematic XY model can be described by the spin stiffness ρ_s [51,52], which characterizes the change of free energy in response to a small uniform phase twist v along a reference direction

$$\rho_s = \left.\frac{\partial^2 f_v}{\partial v^2}\right|_{v=0} = -\frac{1}{N\beta}\left[\frac{1}{Z_v}\frac{\partial^2 Z_v}{\partial v^2} - \left(\frac{1}{Z_v}\frac{\partial Z_v}{\partial v}\right)^2\right]_{v=0} \quad \text{(D1)}$$

where $f_v = -\frac{1}{N\beta}\ln Z_v$ is the free energy per site.

Since the two components of ϕ and θ are coupled together via a relevant intercomponent term, the contribution of the total spin stiffness of both fields should be taken into account. To preserve the $U(1)\times Z_3$ invariance of the model, the phase twist should be applied as

$$(\phi_i, \theta_i) \to (\phi_i + \vec{v}\cdot\vec{r}_i, \theta_i + 3\vec{v}\cdot\vec{r}_i), \quad \text{(D2)}$$

where $\vec{r}_i$ is the position vector for the lattice site i and $\vec{v}$ is a constant vector to increase the phase difference across each neighboring hexatic spins three times larger than nematic spins. When a global twist is applied along the y axis, the phase differences between two nearest-neighbor sites in the y direction are increased by v for ϕ field and $3v$ for θ field, and the corresponding Hamiltonian is changed as

$$\begin{aligned} H_v = &-\Delta\sum_{\langle i,j\rangle_x}\cos(\phi_i-\phi_j) - (2-\Delta) \\ &\times \sum_{\langle i,j\rangle_x}\cos(\theta_i-\theta_j) - \lambda\sum_i\cos(\theta_i-3\varphi_i) \\ &- \Delta\sum_{\langle i,j\rangle_y}\cos(\phi_i-\phi_j+v) \\ &- (2-\Delta)\sum_{\langle i,j\rangle_x}\cos(\theta_i-\theta_j+3v). \end{aligned} \quad \text{(D3)}$$

At the same time, the TN representation of the partition function is modified as

$$Z_v = \mathrm{tTr}\prod_i (O_v)^{n_3m_3,n_4m_4}_{n_1m_1,n_2m_2}(i), \quad \text{(D4)}$$

where an additional phase factor is appended on the vertical leg of the local tensor:

$$(O_v)^{n_3m_3,n_4m_4}_{n_1m_1,n_2m_2} = e^{i(n_1+3m_1)v} O^{n_3m_3,n_4m_4}_{n_1m_1,n_2m_2}. \quad \text{(D5)}$$

The precision of the direct second differentiation on the partition function often suffers from a finite differentiation step v. Alternatively, the calculations of the spin stiffness can be improved by directly contracting the TN containing the differentiated terms independent of v. The first derivative of the partition function with respect to v introduces an impurity tensor R in the original TN as displayed in Fig. 9(a), where

$$R^{n_3m_3,n_4m_4}_{n_1m_1,n_2m_2} = \left.\frac{\partial O_v}{\partial v}\right|_{v=0} = i(n_1+3m_1)O^{n_3m_3,n_4m_4}_{n_1m_1,n_2m_2}. \quad \text{(D6)}$$

Because the partition function is expressed as a tensor product of O_v tensors, the second derivative is composed by two parts: two tensors separately differentiated once and one tensor differentiated twice. The configurations for the second derivative are summed in Fig. 9(b), where

$$S^{n_3m_3,n_4m_4}_{n_1m_1,n_2m_2} = \left.\frac{\partial^2 O_v}{\partial v^2}\right|_{v=0} = -(n_1+3m_1)^2 O^{n_3m_3,n_4m_4}_{n_1m_1,n_2m_2}. \quad \text{(D7)}$$

In the previous section, we evaluate the expectation value of two-point observables when two impurity tensors locate along a horizontal or vertical line using the fixed point MPS. However, for the spin stiffness, because two R tensors are located at different rows and columns, we cannot simply contract the whole network by squeezing the 2D TN into a 1D chain. Fortunately, another contraction strategy [53,54] has been proposed, which is based on the channel environment where the linear fixed points can be bent into corner-shaped transfer matrices as the effective corner environment in approximation to infinite quarter-planes as depicted in Fig. 9(c). The fixed-point equation for the top left corner is shown in Fig. 9(d), where the corner-shaped environment is approximated by a bent MPS comprised of two half infinite boundary MPS connected by an corner matrix K. Once the corner-shaped fixed points in different quarter planes are obtained, arbitrary two-point expectation values can be calculated by contracting the network containing R_i and R_j from four corners. Finally, the network is reduced into the shape of a cross as shown in Fig. 9(e) with the help of the fixed-point eigenvectors F_L and F_R.

All contributions of different configurations of the R tensors should be taken into consideration, which is achieved by moving the R tensors independently in horizontal and vertical directions. The sum of the infinite geometric series of two observables is a bit more involved. For exponentially decaying observables, long-range observables can be evaluated by inverting the corresponding channel operator as a sum of

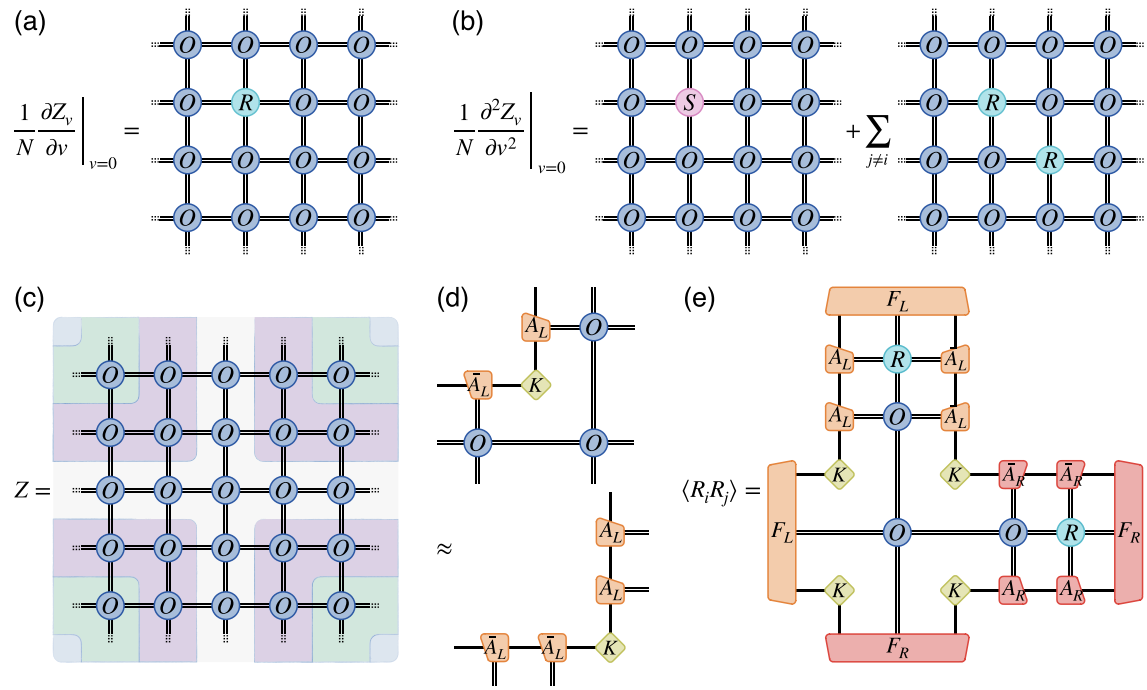

FIG. 9. (a) The tensor network representation of the first derivative of the partition function. (b) The tensor network representation of the second derivative of the partition function. (c) The contraction of an infinite tensor network using corner environments from four corners. (d) The eigenequation of the top left corner-shaped fixed point. (e) The computation of a two-point function expressed by contracting the channel operators and the corner tensors.

channel operators,

$$\sum_{n=0}^{\infty} \mathbb{T}_L^n \simeq [\mathcal{I} - (\mathbb{T}_L - |F_r\rangle\langle F_L|)]^{-1}, \tag{D8}$$

where F_r is the right dominant eigenvector of $\mathbb{T}_L$ whose dominant eigenvalue is renormalized to 1.

The discontinuous jump of the spin stiffness is a characteristic feature for unbinding of topological defects above the BKT transition. In the main text, we show the two-step jump of the superfluid stiffness for both hexatic ($\Delta < 1$) and nematic ($\Delta > 1$) regime. In contrast to the case for small Δ where the stiffness develops a cusp point with a small jump at the lower transition temperature due to the unbinding of vortices with charge $q_\phi = 1$, in the large Δ regime the stiffness drops dramatically at the lower transition temperature T_{c1}. The different behavior of the stiffness jump at lower transition temperatures between small and large Δ cases should be related to the dissociations of different kinds of vortices in the ϕ and θ fields. Since the phase twist v is applied to the hexatic θ field three times larger than to the nematic ϕ field, the ratio of the contribution to the total stiffness is roughly $\Delta : 9(2 - \Delta)$ between ϕ and θ fields for a weak coupling λ [21]. That is why the first drop of the stiffness is almost six times larger than the second drop upon increasing temperature along $\Delta = 1.2$. Such a great drop is different from the strongly coupled case with large λ where the topological defects do not result in a jump of the total stiffness but a gradual decrease at the lower crossover. Further investigations into the correlation properties tells us that the extremely weak coherence between vortices in θ field above T_{c1} should account for the dramatic jump in total stiffness even though the θ field still remains quasi-LRO.

APPENDIX E: CORRELATION FUNCTIONS AND THEIR CORRELATION LENGTHS

To reveal the nature of the topological excitations in different phases, we calculate various two-point correlation functions and the corresponding correlation lengths. Here, we present more details for the correlation properties for intra- and intercomponent observables. Our results are discussed in the hexatic ($\Delta < 1$) and nematic ($\Delta > 1$) regimes, separately.

The correlation functions for $\Delta = 0.8$ are summarized in Fig. 10 and the corresponding correlation lengths are displayed in the first column of Fig. 12.

In the $T = 0.6J$ column below T_{c1}, the intracomponent correlation functions $G_\phi(r)$ in Fig. 10(a) and $G_\theta(r)$ in Fig. 10(g) display the algebraic behavior, indicating the bindings of $q_\phi = 1$ and $q_\theta = 1$ vortices in the ϕ and θ fields, respectively. Moreover, the power-law behavior of $G_{\phi\theta}(r)$ in Fig. 10(j) implies that the vortices and antivortices also bind in the interfield. Therefore, a fully phase-coherent state of the coupled system is established in the low-temperature phase. Besides, the intercomponent Potts variable develops a true LRO and the correlation function $G_\sigma(r)$ in Fig. 10(m) becomes a constant for large r.

In the $T = 1.0J$ column of the intermediate temperatures, the most interesting physics happens in the ϕ field. When cooling down the system from the high-temperature disordered phase, the buildup of correlations in the θ field first occurs at T_{c2} with an algebraically decaying correlation func-

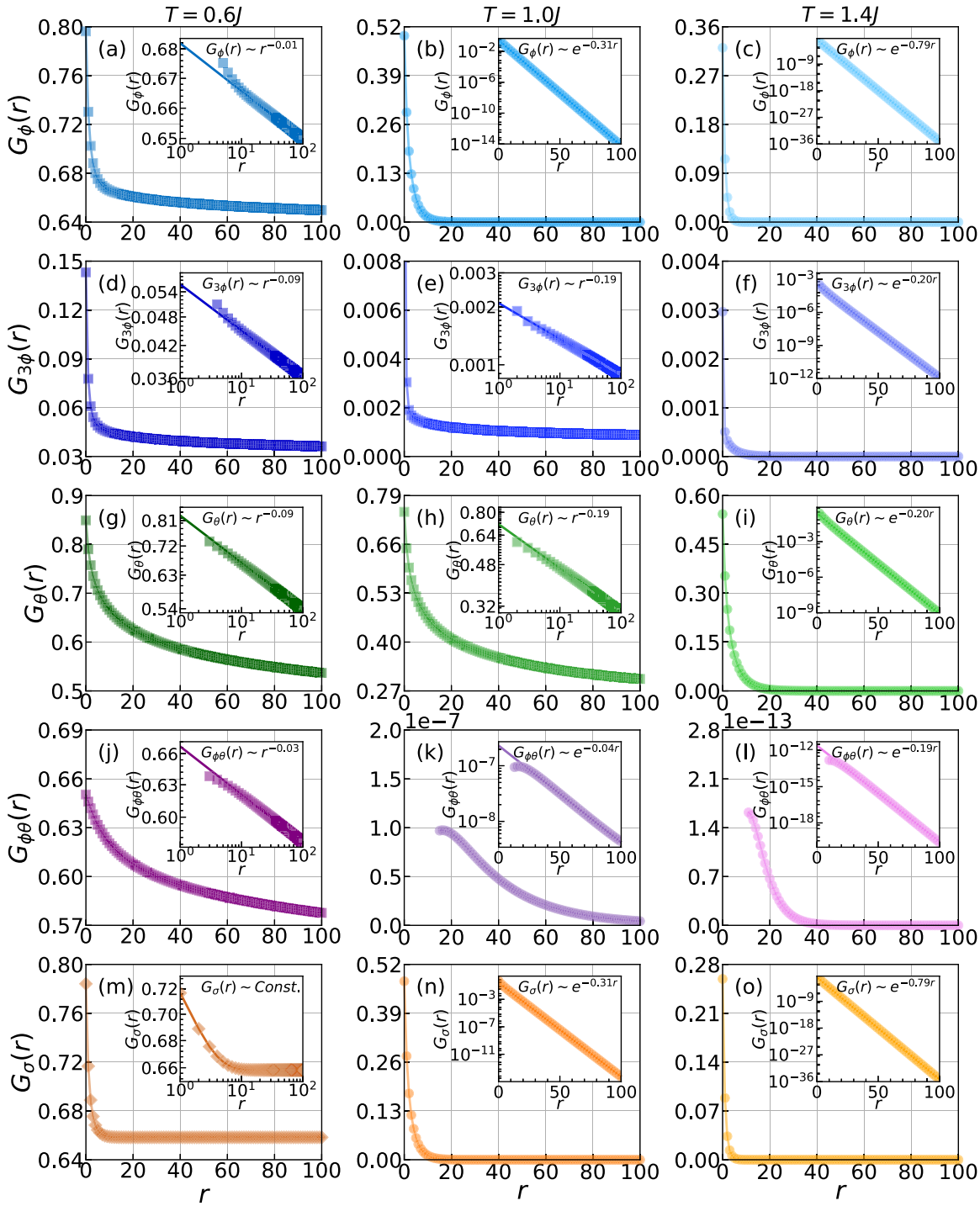

FIG. 10. Various two-point correlation functions are calculated under the intracomponent coupling ratio $\Delta = 0.8$ and the intercomponent coupling $\lambda = 0.1$. Different columns denote different values of $T = 0.6J$, $1.0J$, and $1.4J$ as indicated.

tion $G_\theta(r)$ in Fig. 10(h), corresponding to the binding of hexatic vortices with charge $q_\theta = 1$. For the fractional vortex paired phase between T_{c1} and T_{c2}, the correlation function $G_\phi(r)$ decays exponentially, while the correlation function $G_{3\phi}(r)$ of the fractionalized vortices exhibit an algebraic behavior.

As displayed in Figs. 10(b) and 10(e), the direct comparison between difference correlation behaviors demonstrates that the integer nematic vortices $q_\phi = 1$ in the ϕ field are fractionalized into fractional nematic vortices with $q_\phi = 1/3$ due to the presence of the intercomponent Z_3 degrees of freedom. Since the fractional nematic vortices are pointlike topological defects around which the phase angles of spins wind by $2\pi/3$, each fractional nematic vortices should be at the end of a domain-wall string across which the ϕ field twists by $2\pi/3$. The existence of multiple Potts domains destroys the phase

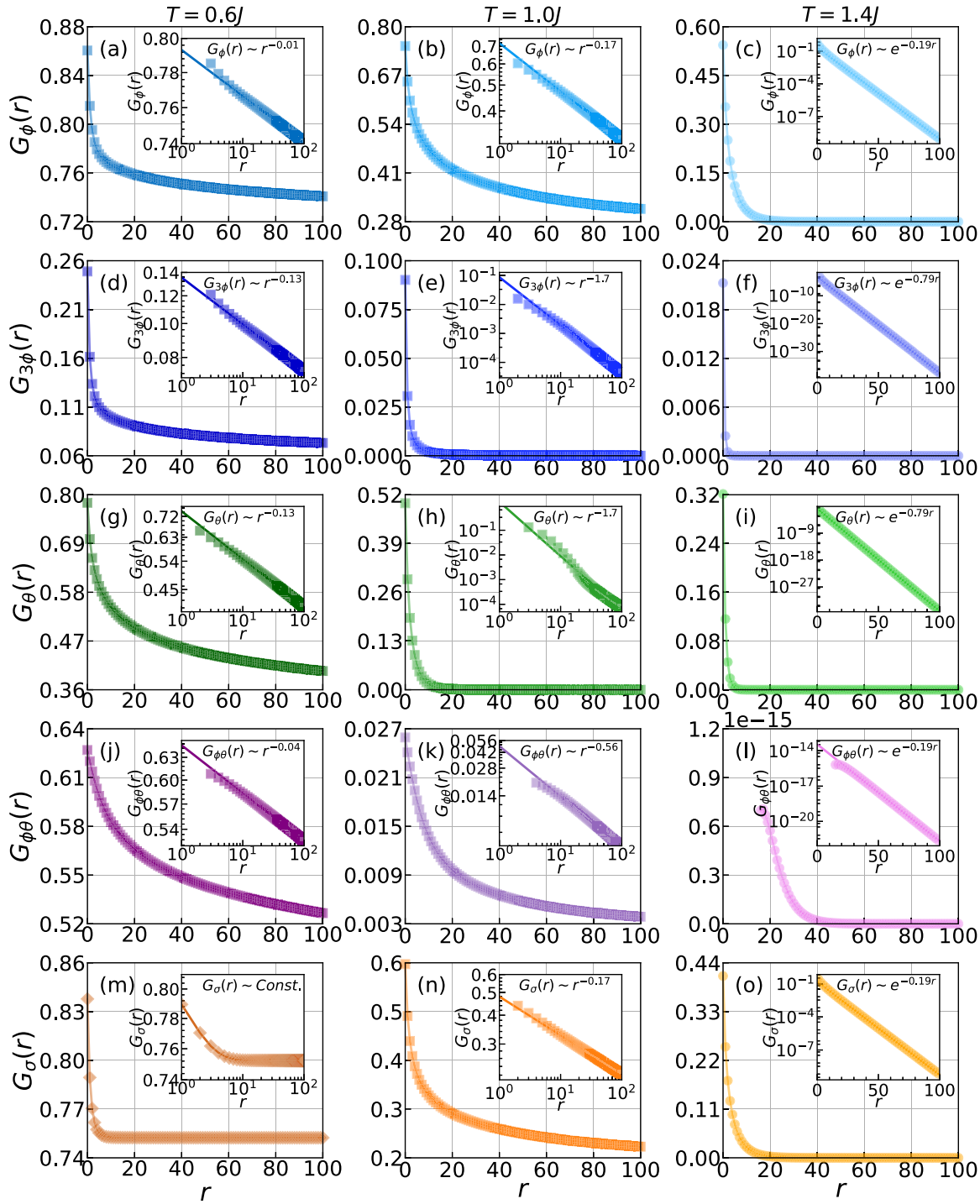

FIG. 11. Various two-point correlation functions are calculated under the intracomponent coupling ratio $\Delta = 1.2$ and the intercomponent coupling $\lambda = 0.1$. Different columns denote different values of $T = 0.6J$, $1.0J$, and $1.4J$ as indicated.

coherence in the ϕ field and leads to disorder in intercomponent σ variables. As we can see, both $G_{\phi\theta}(r)$ in Fig. 10(k) and $G_\sigma(r)$ in Fig. 10(n) display the exponential decay. We should point out that the correlation length ξ_ϕ extracted from $G_\phi(r)$ could be fitted by an exponentially divergent form $\xi(T) \propto \exp(b/\sqrt{T - T_C})$ above T_{c1} as shown in Fig. 12(a) with $b > 0$ as a key feature of the BKT transition, which implies that the transition at T_{c1} is a hybrid BKT and Potts transition. Furthermore, as shown in Fig. 12(e), the correlation length ξ_σ for the intercomponent Potts variable extracted from

$$e^{-r/\xi_\sigma} \propto \langle \cos(\sigma_i - \sigma_{i+r}) \rangle - \langle \cos(\sigma_i) \rangle \langle \cos(\sigma_{i+r}) \rangle \tag{E1}$$

is well fitted by $\xi_\sigma \propto 1/|T - T_{c1}|^{5/6}$ in agreement with 2D Potts universality class.

In the $T = 1.4J$ column above T_{c2}, all the correlation functions decay exponentially and the system is disordered.

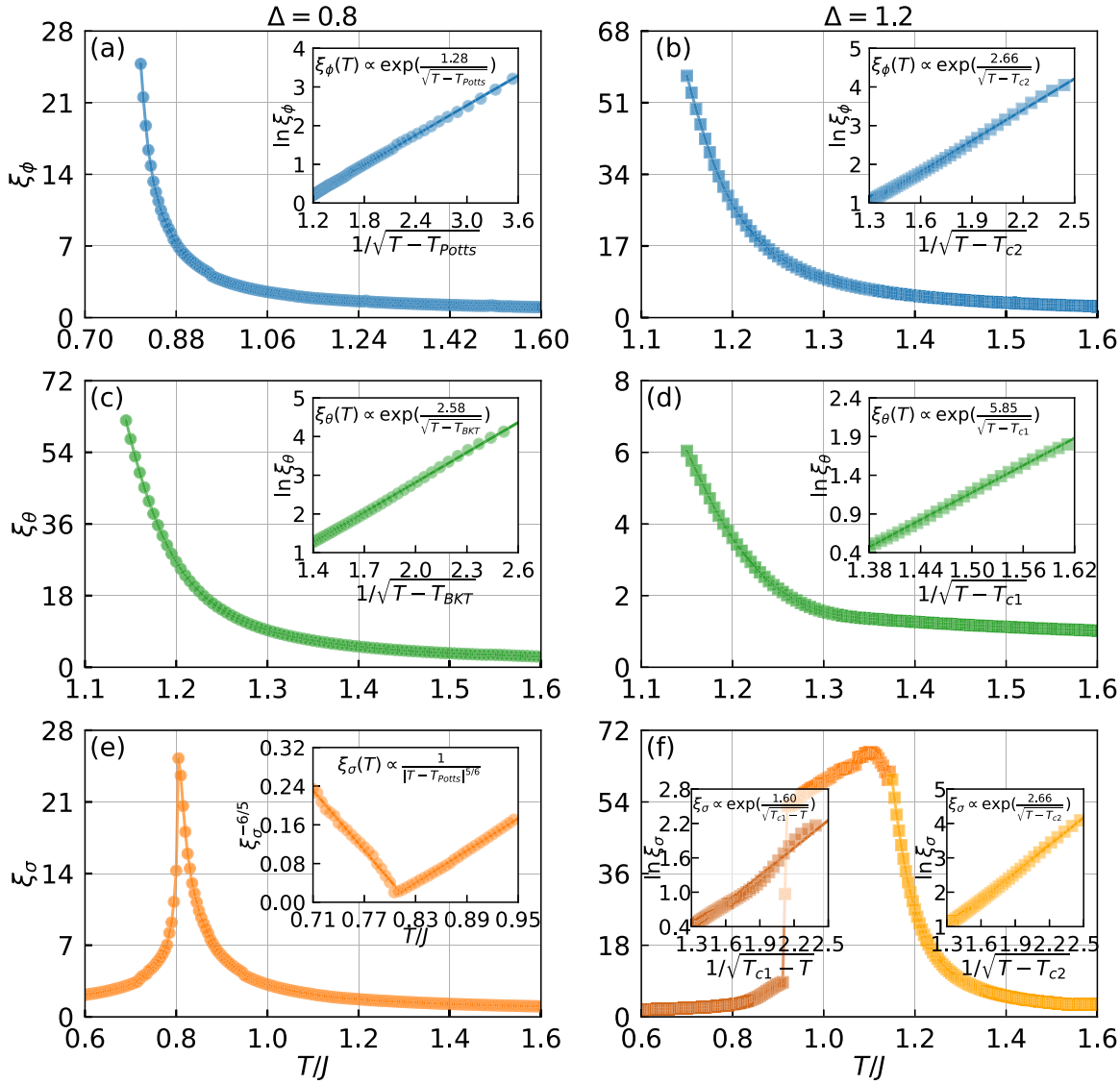

FIG. 12. Different correlation lengths ξ_ϕ, ξ_θ, and ξ_σ are calculated for nematic ϕ, hexatic θ, and intracomponent σ under $\lambda = 0.1$, respectively. Different columns denote different values of $\Delta = 0.8$ and $\Delta = 1.2$ as indicated.

When approaching T_{c2} from high temperatures, the relevant correlation length ξ_θ is extracted and displayed in Fig. 12(c), which can be well fitted by an exponentially divergent form of the BKT transition.

It is interesting to see that the correlation functions of $G_\theta(r)$ and $G_{3\phi}(r)$ share the same exponents while $G_\phi(r)$ and $G_\sigma(r)$ share the same exponents. Such behavior can be interpreted as another proof of the relevance of the intercomponent couplings. Due to the relative locking, the θ and 3ϕ fields have the same long-wavelength behavior and the correspondence $q_\theta = 3q_\phi$ between vortex charges is established.

However, the correlation functions for $\Delta = 1.2$ are summarized in Fig. 11 and the corresponding correlation lengths are displayed in the second column of Fig. 12.

In the $T = 0.6J$ column below T_{c1}, all intracomponent correlation functions show a power-law behavior and the correlation function for the intercomponent Potts variable becomes a constant for long distance as displayed in Fig. 11(m). In fact, the low-temperature phases in the hexatic and nematic regime share the same physics.

In the $T = 1.0J$ column of the intermediate temperatures, the power-law behavior of $G_\theta(r)$ in Fig. 11(h) demonstrates that the quasi-LRO in the θ field survives through the transition at T_{c1}. A direct comparison between the amplitude of $G_\theta(r)$ at two sides of T_{c1} in the main text shows that the coherence between spins in the θ field is greatly suppressed by three orders of magnitude across the transition at T_{c1}. Although the θ field is still quasi-LRO, the extremely weak coherence above T_{c1} could account for the dramatic jump in total stiffness at T_{c1}. The reason for the absence of the unbinding transition in the θ field is that the onset of algebraic correlations in the ϕ field in Fig. 11(b) leads to the quasi-LRO in the θ field because they are coupled by the relevant intercomponent term $\lambda\cos(\theta_i - 3\phi_i)$. Since the vortices with charge $q_\phi = 1$ in the ϕ field are bound below T_{c2}, the dominant topological excitations in the θ field between T_{c1} and T_{c2} should be composite

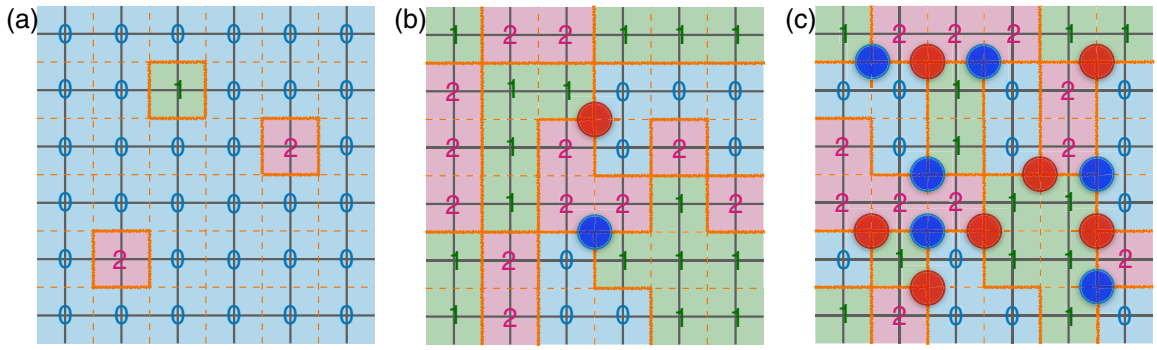

FIG. 13. Schematic representations of the topological defects of the Z_3 variables in (a) the Potts ordered phase, (b) the Potts liquid phase, and (c) the Potts disordered phase, respectively. The Potts variables ($\sigma_i = 0, 1, 2$) are defined on the original lattice while domain walls (orange thick lines), vortices (red dots), and antivortices (blue dots) are defined on the dual lattice.

vortex pairs with $q_\theta = 3$. Moreover, the composite $q_\theta = 3$ vortices should further fractionalize into three $q_\theta = 1$ vortices bound together as a larger extended vortex core to lower the gradient energy cost, especially for weakly coupled cases of smaller λ. In this way, the correlation $G_\theta(r)$ should be viewed as a higher order expansion of the correlation function among composite vortices, which has the same long-wavelength behavior as $G_\phi(r)$.

In the $T = 1.4J$ column above T_{c2}, all the correlation functions decay exponentially and the system is disordered. When approaching T_{c2} from high temperatures, the corresponding correlation length ξ_ϕ for $G_\phi(r)$ as well as ξ_θ for $G_\theta(r)$ are extracted and displayed in Figs. 12(b) and 12(d), respectively. Both ξ_ϕ and ξ_θ above T_{c2} can be well fitted by an exponentially divergent form of the BKT transition.

The most interesting physics is revealed in further investigations into the intercomponent Potts variable σ_i. In the strongly coupled case of large λ, the LRO of σ is found to be lost at T_{c2} together with the destruction of the quasi-LRO in both the hexatic and nematic fields through a BKT transition. However, for the weekly coupled case, the order-disorder transition in σ variables splits into two transitions separated by an intermediate phase with Potts quasi-LRO, which is regarded as the Potts liquid phase. As shown in Figs. 11(m)–11(o), the correlation function $G_\sigma(r)$ exhibits a constant value, an algebraic decay, and an exponential decay at $T = 0.6J$, $T = 1.0J$, and $T = 1.4J$, respectively. Such unconventional two-stage phase transitions should be associated with the separated proliferations of the Z_3 domain walls and Z_3 vortices, similar to two continuous phase transitions in the Z_p clock models with $p > 4$. The correlation length ξ_σ is also extracted from $e^{-r/\xi_\sigma} \propto \langle\cos(\sigma_i - \sigma_{i+r})\rangle - \langle\cos(\sigma_i)\rangle\langle\cos(\sigma_{i+r})\rangle$ as displayed in Fig. 12(f). The similar behavior of the correlation length was also observed in p-state clock models ($p > 4$) [29]. For the clock model, the correlation lengths scale exponentially with T when the quasi-LRO phase is approached from both the ordered and disordered sides, which means that both the transitions at lower and higher temperatures belong to the BKT class. However, as displayed in the inset of Fig. 12(f), the correlation length for $T > T_{c2}$ (right inset) agrees well with the BKT behavior while for $T < T_{c1}$ (left inset) the correlation length cannot fit well in the exponential form. Therefore, it is reasonable to infer that the phase transition at T_{c1} slightly deviates from the standard BKT class.

APPENDIX F: TOPOLOGICAL DEFECTS IN Z_3 VARIABLES

To illustrate the splitting of the order-disorder transition in the Z_3 Potts variables, the corresponding topological defects are schematic depicted in Fig. 13. Unlike the 2D Ising model where a phase transition is driven by looplike domain walls, the Z_3 Potts model allows the looplike domain walls as well as Z_3 vortices. The Z_3 Potts variables $\sigma_i = 0, 1, 2$ are defined at each vertex on a square lattice (black lines). The topological defects, Z_3 domain walls and vortices, are defined on the dual lattice (orange dotted line). Each segment of the domain wall corresponds to a mismatch in the Potts variables across the edge. The Z_3 vortices are determined by the vorticity around the vertex of the dual lattice

$$\omega_p = \frac{1}{3} \sum_{\langle i,j\rangle \in \square_p} \Delta_{ij}, \tag{F1}$$

where $\Delta_{ij} = \sigma_i - \sigma_j$ are wrapped within $[-1, +1]$ surrounding the plaquette anticlockwise.

For the conventional Potts model, only a single Potts transition is observed because the proliferation of two kinds of topological defects are coupled together. However, we find that a quasi-LRO intermediate phase can appear in the Z_3 Potts variables due to the separated excitations of different topological defects in the weakly coupled model. The low-temperature transition is driven by the proliferation of domain walls while the high-temperature transition results from excitations of free Z_3 vortices. The effective core energy of Z_3 vortices in the σ field of the coupled hexatic-nematic model could be increased by a finite inter-component coupling. Actually, a finite λ makes it more costly for the excitations of free vortices in the θ field which would proliferate through a BKT transition at T_{c1} if $\lambda = 0$. On the other hand, for large λ limit, the energy of domain walls increases dramatically which forbids the excitations of domain walls before the proliferation of free Z_3 vortices and only one transition is left. Since the σ variable is determined by the θ and ϕ field simultaneously, the relation between the intercomponent coupling λ and core energy of Z_3 vortices is more complicated. An estimation made from an

effective long-wavelength model [21] gives that the energies of domain walls are proportional to $\sqrt{\lambda\Delta}$ while the core energies of the vortices in the phase field are proportional to Δ. Therefore, a small λ is required in the coupled hexatic-nematic model to achieve a relatively high ratio of the core energy of the Z_3 vortices compared to domain walls. An investigation of the changes of the phase structure on different λ is presented in the main text.

[1] V. L. Berezinskii, Sov. Phys. JETP **32**, 493 (1971).
[2] J. M. Kosterlitz and D. J. Thouless, J. Phys. C **6**, 1181 (1973).
[3] J. M. Kosterlitz, J. Phys. C **7**, 1046 (1974).
[4] B. I. Halperin and D. R. Nelson, Phys. Rev. Lett. **41**, 121 (1978).
[5] D. R. Nelson and B. I. Halperin, Phys. Rev. B **19**, 2457 (1979).
[6] A. P. Young, Phys. Rev. B **19**, 1855 (1979).
[7] J. M. Kosterlitz, Rep. Prog. Phys. **79**, 026001 (2016).
[8] V. N. Ryzhov, E. E. Tareyeva, Y. D. Fomin, and E. N. Tsiok, Phys. Usp. **60**, 857 (2017).
[9] K. J. Strandburg, Rev. Mod. Phys. **60**, 161 (1988).
[10] E. P. Bernard and W. Krauth, Phys. Rev. Lett. **107**, 155704 (2011).
[11] S. C. Chae, N. Lee, Y. Horibe, M. Tanimura, S. Mori, B. Gao, S. Carr, and S.-W. Cheong, Phys. Rev. Lett. **108**, 167603 (2012).
[12] L. Radzihovsky, P. B. Weichman, and J. I. Park, Ann. Phys. **323**, 2376 (2008).
[13] F. Shahbazi and R. Ghanbari, Phys. Rev. E **74**, 021705 (2006).
[14] L. de Forges de Parny, A. Rançon, and T. Roscilde, Phys. Rev. A **93**, 023639 (2016).
[15] P. Serna, J. T. Chalker, and P. Fendley, J. Phys. A: Math. Theor. **50**, 424003 (2017).
[16] M. Kobayashi, M. Eto, and M. Nitta, Phys. Rev. Lett. **123**, 075303 (2019).
[17] R. Bruinsma and G. Aeppli, Phys. Rev. Lett. **48**, 1625 (1982).
[18] G. Aeppli and R. Bruinsma, Phys. Rev. Lett. **53**, 2133 (1984).
[19] I. M. Jiang, S. N. Huang, J. Y. Ko, T. Stoebe, A. J. Jin, and C. C. Huang, Phys. Rev. E **48**, R3240 (1993).
[20] I. M. Jiang, T. Stoebe, and C. C. Huang, Phys. Rev. Lett. **76**, 2910 (1996).
[21] V. Drouin-Touchette, P. P. Orth, P. Coleman, P. Chandra, and T. C. Lubensky, Phys. Rev. X **12**, 011043 (2022).
[22] F. Verstraete, V. Murg, and J. Cirac, Adv. Phys. **57**, 143 (2008).
[23] R. Orús, Ann. Phys. **349**, 117 (2014).
[24] J. Haegeman and F. Verstraete, Annu. Rev. Condens. Matter Phys. **8**, 355 (2017).
[25] V. Zauner-Stauber, L. Vanderstraeten, M. T. Fishman, F. Verstraete, and J. Haegeman, Phys. Rev. B **97**, 045145 (2018).
[26] M. T. Fishman, L. Vanderstraeten, V. Zauner-Stauber, J. Haegeman, and F. Verstraete, Phys. Rev. B **98**, 235148 (2018).
[27] L. Vanderstraeten, J. Haegeman, and F. Verstraete, SciPost Phys. Lect. Notes 7 (2019).
[28] L. Vanderstraeten, B. Vanhecke, A. M. Läuchli, and F. Verstraete, Phys. Rev. E **100**, 062136 (2019).
[29] Z.-Q. Li, L.-P. Yang, Z. Y. Xie, H.-H. Tu, H.-J. Liao, and T. Xiang, Phys. Rev. E **101**, 060105(R) (2020).
[30] F.-F. Song and G.-M. Zhang, Phys. Rev. Lett. **128**, 195301 (2022).
[31] E. Granato and J. M. Kosterlitz, Phys. Rev. B **33**, 4767 (1986).
[32] F. C. Poderoso, J. J. Arenzon, and Y. Levin, Phys. Rev. Lett. **106**, 067202 (2011).
[33] G. A. Canova, Y. Levin, and J. J. Arenzon, Phys. Rev. E **89**, 012126 (2014).
[34] G. A. Canova, Y. Levin, and J. J. Arenzon, Phys. Rev. E **94**, 032140 (2016).
[35] F.-F. Song and G.-M. Zhang, Phys. Rev. B **103**, 024518 (2021).
[36] F.-F. Song and G.-M. Zhang, Phys. Rev. B **105**, 134516 (2022).
[37] G. Vidal, J. I. Latorre, E. Rico, and A. Kitaev, Phys. Rev. Lett. **90**, 227902 (2003).
[38] F. Pollmann, S. Mukerjee, A. M. Turner, and J. E. Moore, Phys. Rev. Lett. **102**, 255701 (2009).
[39] D. M. Hübscher and S. Wessel, Phys. Rev. E **87**, 062112 (2013).
[40] F. Y. Wu, Rev. Mod. Phys. **54**, 235 (1982).
[41] M. B. Einhorn, R. Savit, and E. Rabinovici, Nucl. Phys. B **170**, 16 (1980).
[42] S. Bhattacharya and P. Ray, Phys. Rev. Lett. **116**, 097206 (2016).
[43] R. Pindak, D. E. Moncton, S. C. Davey, and J. W. Goodby, Phys. Rev. Lett. **46**, 1135 (1981).
[44] C. C. Huang, J. M. Viner, R. Pindak, and J. W. Goodby, Phys. Rev. Lett. **46**, 1289 (1981).
[45] C.-F. Chou, A. J. Jin, S. W. Hui, C. C. Huang, and J. T. Ho, Science **280**, 1424 (1998).
[46] D. R. Nelson and B. I. Halperin, Phys. Rev. B **21**, 5312 (1980).
[47] E. A. Donley, N. R. Claussen, S. T. Thompson, and C. E. Wieman, Nature (London) **417**, 529 (2002).
[48] C. Chin, R. Grimm, P. Julienne, and E. Tiesinga, Rev. Mod. Phys. **82**, 1225 (2010).
[49] R. M. Fernandes, L. H. VanBebber, S. Bhattacharya, P. Chandra, V. Keppens, D. Mandrus, M. A. McGuire, B. C. Sales, A. S. Sefat, and J. Schmalian, Phys. Rev. Lett. **105**, 157003 (2010).
[50] R. M. Fernandes, P. P. Orth, and J. Schmalian, Annu. Rev. Condens. Matter Phys. **10**, 133 (2019).
[51] M. E. Fisher, M. N. Barber, and D. Jasnow, Phys. Rev. A **8**, 1111 (1973).
[52] D. R. Nelson and J. M. Kosterlitz, Phys. Rev. Lett. **39**, 1201 (1977).
[53] L. Vanderstraeten, M. Mariën, F. Verstraete, and J. Haegeman, Phys. Rev. B **92**, 201111(R) (2015).
[54] L. Vanderstraeten, J. Haegeman, P. Corboz, and F. Verstraete, Phys. Rev. B **94**, 155123 (2016).